Transfer line including vacuum differential system for a high-power windowless target

Yuanshuai Qin, Peng Zhang, Hanjie Cai, Yaling Zhang, Huan Jia,* Chenzhang Yuan, Yuan He, Junhui Zhang, and Wenlong Zhan

Institute of Modern Physics, Chinese Academy of Sciences, Lanzhou 730000, People's Republic of China

(Received 8 March 2020; accepted 8 September 2020; published 17 November 2020)

As the highest power proton linear accelerator in continuous wave mode, China initiative Accelerator Driven sub-critical System linear accelerator will deliver 2.5 MW proton beam to the target inside the reactor. Vacuum transition from 5×10^4 Pa to several 10^{-6} Pa is required at the accelerator to target section. A vacuum differential system located at the transfer line is designed to meet the requirement of the windowless target and upstream collimators are considered for power loss control in this paper. A vacuum test based on vacuum transition verifies that about 10 orders of magnitude vacuum transition could be achieved as required, and gas scattering simulation shows that the power loss and beam size increase are at an acceptable level before the last magnet.

DOI: 10.1103/PhysRevAccelBeams.23.113002

I. INTRODUCTION

China initiative Accelerator Driven subcritical System (CiADS) project was approved by the Chinese government, aiming to demonstrate the nuclear waste transmutation, including a superconducting (SC) linear accelerator (linac), a high-power target, and a reactor. The accelerated proton beam will hit the target to produce high-flux neutrons to boost the transmutation of nuclear waste in the reactor [1].

The SC linac of CiADS will be operated at 2 K temperature and the beam power will reach 2.5 MW with the energy of 500 MeV and the current of 5 mA in continuous wave (CW) mode (as shown in Table I) [2], with the potential for upgrading to 1 GeV or even higher energy in the future, as shown in Fig. 1. The main accelerator structure is SC cavities, and the vacuum should be at the level of several 10^{-6} Pa. The accelerator to target (A2T) section is designed to deliver the high-power beam to the target and meet the requirement of vacuum transition meanwhile. The beam is bent horizontally 90° and then vertically 90° to match the target inside the reactor, with local achromatic design.

In the long horizontal transport section, there are collimation section and vacuum differential system (VDS) section. The dispersion function is zero in the collimation section, as shown in Figs. 2 and 3.

For the high-power target, the vacuum environment at the target section is far higher than that in the SC section and the vacuum should be separated between them, i.e., vacuum transition. According to the requirement of CiADS target [dense granular target (DGT)[3] or liquid lead bismuth eutectic (LBE)], it is filled with helium gas in 5×10^4 Pa pressure. Thus, about 10 orders magnitude for vacuum transition needs to be achieved in the A2T section.

Target with beam window is an effective way to realize vacuum transition, as that has been designed and operated at SNS [4,5], J-PARC [6,7], CSNS [8–10], and PSI [11,12]. The main challenge for beam windows is the high-power heat deposition and related cooling and shielding. Another problem is the lifetime of the window and related maintenance and replacement after long term exposure in the proton and neutron radiation environment, especially for high-power accelerator and target. According to the experience of MEGAPIE, with additional electromagnetic pumps (EMPs) providing bypass jet flow for the beam window cooling [13], the highest temperature achieved on the beam window is 350 °C with 1 MW power beam [14]. Based on the irradiation experiment of T91 material, the

TABLE I. Beam parameters in the linac of CiADS.

Parameters	Value	Unit
Particle	Proton	…
Energy	500	MeV
Average current	5	mA
Duty factor	100	%
Power	2.5	MW

*Corresponding author.
jiahuan@impcas.ac.cn

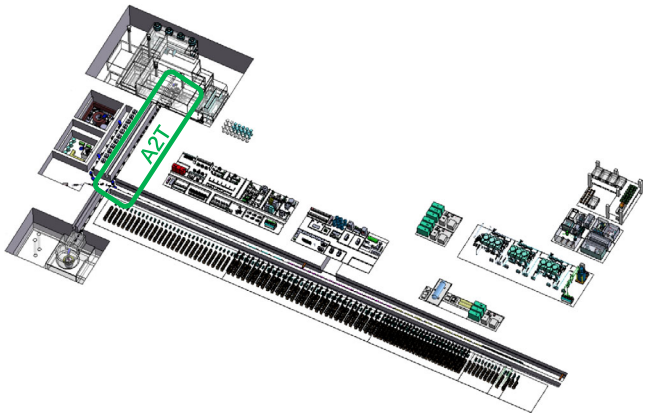

FIG. 1. The layout of the CiADS accelerator.

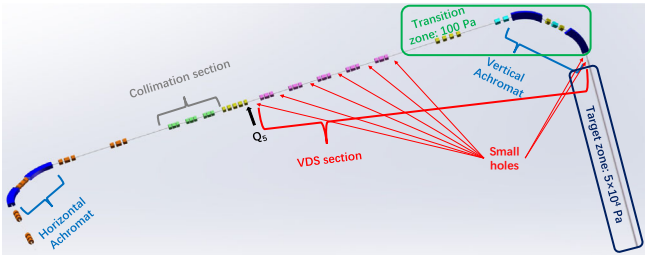

FIG. 2. CiADS A2T layout including VDS.

lifetime of the beam window is limited to be less than 6.8 DPA (displacement-per-atom)[15]. For beam current density of 35 μA/cm^2, the lifetime of the beam window is about 3 months with proton energy of 590 MeV [16], which is similar to the proton energy in CiADS. The average proton beam current (5 mA) at CiADS is 2.8 times of that in MEGAPIE (1.8 mA), but if the beam current density is also limited within 35 μA/cm^2 for CiADS, the lifetime of the beam window will be the same as 3 months level.

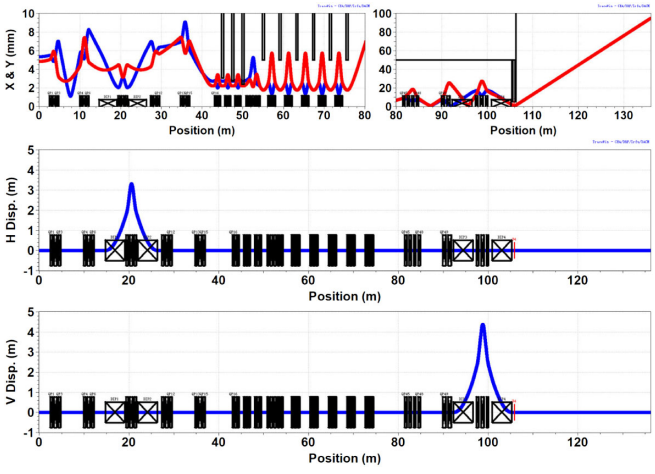

FIG. 3. 5σ envelope and dispersion function at CiADS A2T section. (The maximum dispersion function is about $D_x = 3.3$ m and $D_y = 4.4$ m).

To avoid the problems accompanied by the beam window, a vacuum differential system in A2T is proposed for windowless target design of CiADS. The main challenge of VDS is to avoid beam loss on the small vacuum differential holes, thus a collimation system upstream is considered.

In this paper, first, since the vacuum transition is achieved by multistage small holes, beam dynamics are studied and optimized in the code TRACEWIN [17], including the VDS section and upstream collimation section. Second, for the beam in 5×10^4 Pa at the target zone and 100 Pa at the transition zone (as shown in Fig. 2), the gas scattering effect between the proton beam and the helium gas is simulated to check beam size increase and power losses in the beam tube. Third, a vacuum differential test bench is built to verify the feasibility of VDS.

II. BEAM DYNAMICS

Since the vacuum pressure varies from 10^{-6} Pa to 10^4 Pa, all the three types of flow are presented in the VDS. For a tube or hole, the effect of vacuum transition depends on the pressure difference [18]:

$$\Delta p = \frac{Q}{C}, \tag{1}$$

where $C = \frac{1}{6}\sqrt{\frac{2\pi RT}{M}} \cdot \frac{d^3}{L}$ and $C = \sqrt{\frac{2\gamma}{\gamma-1}\frac{RT}{M}} \cdot x^{\frac{1}{\gamma}}\sqrt{1-x^{\frac{\gamma-1}{\gamma}}} \cdot \frac{1}{1-x}\frac{\pi}{4} \cdot d^2$ are the conductance for molecular flow in a long tube and viscous flow in a thin hole respectively [19], where d is the diameter and L is the length of the tube. Knudsen flow is between molecular flow and viscous flow and the conductance for molecular flow is adopted to make a conservative estimation of Knudsen flow in the design, i.e., $C = \sqrt{\frac{RT}{2\pi M}} \cdot \frac{\pi}{4} \cdot d^2$. It indicates that reducing the diameter or increasing the length of the tube are beneficial for the vacuum transition, where reducing the diameter is more effective for molecular flow in a long tube. In beam dynamics, a beam waist with a small root mean square (RMS) beam size in both horizontal and vertical planes is needed to avoid beam losses at the vacuum differential holes.

A. Beam from linac

The beam coming out from the linac can be considered as a Gaussian beam. For two-dimensional Gaussian distribution $(X, Y) \sim N(\mu_x, \mu_y, \sigma_x^2, \sigma_y^2, r)$, the distribution function is

$$f(\mu_x, \mu_y, \sigma_x^2, \sigma_y^2, r) = \frac{1}{\sigma_x \sigma_y \cdot 2\pi\sqrt{1-r^2}} \cdot e^{-\frac{1}{2(1-r^2)}\left[\frac{(x-\mu_x)^2}{\sigma_x^2} - \frac{2r(x-\mu_x)(y-\mu_y)}{\sigma_x\sigma_y} + \frac{(y-\mu_y)^2}{\sigma_y^2}\right]}, \tag{2}$$

TABLE II. Probability density for 2D Gaussian distribution and corresponding beam power. (Missing items indicate too high or too low).

N	Probability density outside $N \cdot \sigma$	2.5 MW beam	5 MW beam	7.5 MW beam
Unit	%	W	W	W
1	60.7	…	…	…
2	13.5	…	…	…
3	1.11	27.8×10^3	55.6×10^3	83.3×10^3
4	3.36×10^{-2}	0.84×10^3	1.68×10^3	2.52×10^3
5	3.73×10^{-4}	9.32	18.6	28.0
6	1.52×10^{-6}	0.0381	0.0762	0.114
7	2.29×10^{-9}	…	…	…

where μ_x, μ_y is the beam center, σ_x, σ_y is the beam RMS size, and r is the correlation coefficient between x and y. In design consideration, the beam shape at the collimators is centered, round, and uncoupled, i.e., $\mu_x = \mu_y = 0$, $\sigma_x = \sigma_y = \sigma$, $r = 0$, then the function is written as $f(0, 0, \sigma^2, \sigma^2, 0) = \frac{1}{2\pi\sigma^2} \cdot e^{-\frac{x^2+y^2}{2\sigma^2}}$, and the probability density inside $N \cdot \sigma$ takes:

$$P = \int_{-N\sigma}^{N\sigma} \int_{-\sqrt{(N\sigma)^2 - x^2}}^{\sqrt{(N\sigma)^2 - x^2}} \frac{1}{2\pi\sigma^2} e^{-\frac{x^2+y^2}{2\sigma^2}} dxdy, \tag{3}$$

and the probability density outside $N \cdot \sigma$ is $1 - P$.

B. Hole aperture selection

Equation (3) cannot be solved analytically, and the numerical solution is shown in Table II. According to the experience of SNS, power loss on collimators should be controlled within the level of several kW [20]. Thus, 4σ is the minimum value that needs to be set at collimators according to Table II. Considering margins and errors, the collimator hole radius is set as 5σ in the collimation section for CiADS.

C. Beam optics in vacuum differential system

It is impossible to achieve almost 10 orders magnitude of the vacuum transition by only one or two thin holes with long tubes in mm level, thus multistage VDS is considered, which means that periodic structure is needed in physical design. Beam size at the middle of two doublets is the same, but one plane is convergent and the other plane is divergent, and the beam size will extend quickly in the divergent plane. In contrast with that, the beam shape between two triplets keeps round and the vacuum differential hole could be just set at the beam waist. Thus, triplet is adopted as the periodic focusing structure in the VDS section.

For a triplet period with the symmetric structure as shown in Fig. 4, beam waist with small RMS envelope is achieved at the beginning and the end of the period.

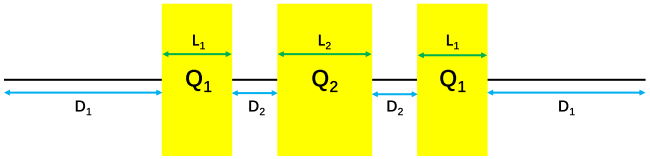

FIG. 4. Triplet sketch.

Considering the limitation of the gradient of quadrupoles, the layout and the thickness of the quadrupoles need to be optimized.

In the energy region of 500 MeV to 1.5 GeV, the space charge effect is not dominant for beam transport and beam size can be considered extending from the waist analytically. Without considering the space charge effect, according to the theory of emittance ellipse transformation [21],

$$\sigma_1 = R\sigma_0 R^T \tag{4}$$

where $R = \begin{bmatrix} 1 & L \\ 0 & 1 \end{bmatrix}$, $R^T = \begin{bmatrix} 1 & 0 \\ L & 1 \end{bmatrix}$ and $\sigma = \begin{bmatrix} \beta & -\alpha \\ -\alpha & \gamma \end{bmatrix}$, the relationship between the beta functions at the waist and the drift end could be written as $\beta_1 = \beta_0 - 2\alpha_0 L + \gamma_0 L^2$. Since the drift is from the beam waist where $\alpha_0 = 0$ and $\gamma_0 = \frac{1+\alpha_0^2}{\beta_0} = \frac{1}{\beta_0}$, then

$$\beta_1 = \beta_0 + \frac{L^2}{\beta_0}, \tag{5}$$

where L is the length of the drift, β_0 and β_1 are beta functions at the waist and the end of the drift. So

$$L = \sqrt{\beta_0 \cdot (\beta_1 - \beta_0)} \tag{6}$$

where $\beta_0 = \frac{\sigma_0^2}{\varepsilon_g} = \frac{\sigma_0^2}{\varepsilon_n/(\beta\gamma)}$ and $\beta_1 = \frac{\sigma_1^2}{\varepsilon_g} = \frac{\sigma_1^2}{\varepsilon_n/(\beta\gamma)}$. Beam RMS size near the waist should be smaller than 0.5 mm, in this case, 10 times RMS envelope would be within 5 mm. The drift length gets the maximum value $L = 0.58$ m for 500 MeV proton beam when

$$\sigma_0 = \frac{\sigma_1}{\sqrt{2}} = \frac{0.5}{\sqrt{2}} \text{mm} \simeq 0.35 \text{ mm} \tag{7}$$

for beam size $\sigma_1 = 0.5$ mm at the end of the drift, and the corresponding beta function at the waist is $\beta_0 = 0.57$ mm$/(\pi \cdot$ mrad$)$, for normalized RMS transverse emittance $\varepsilon_n = 0.25\ \pi \cdot$ mm $\cdot$ mrad.

For matching the same Twiss parameters at the beginning and the end of each period, the gradient of the quadrupoles is adjusted. Considering the limitation of the magnetic field in normal conducting quadrupoles, the gradient of Q_1 and Q_2 should be close to each other. For $\sigma_0 = 0.35$ mm, a simulation script is developed for optimizing the ratio of L_2/L_1, while keeping the gradient of Q_1

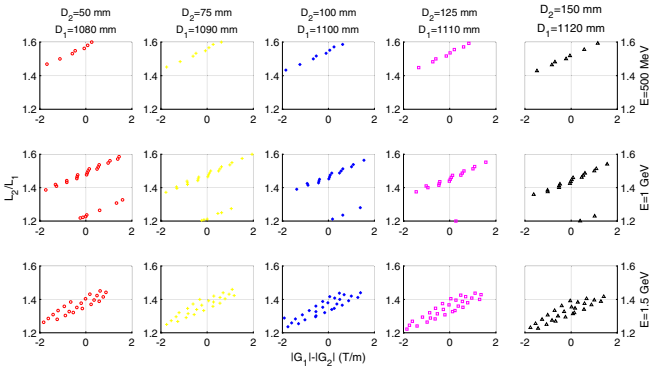

FIG. 5. The ratio of thickness and gradient difference. (G_1 and G_2 indicate the gradient of Q_1 and Q_2, L_1 and L_2 are the thickness of Q_1 and Q_2, D_2 is the drift length between quadrupoles in the triplet, D_1 is the drift length before the first quadrupole in the triplet. In some cases, the distribution is separated into two branches and the lower L_2/L_1 ones are for thicker quadrupoles, which is not preferred.)

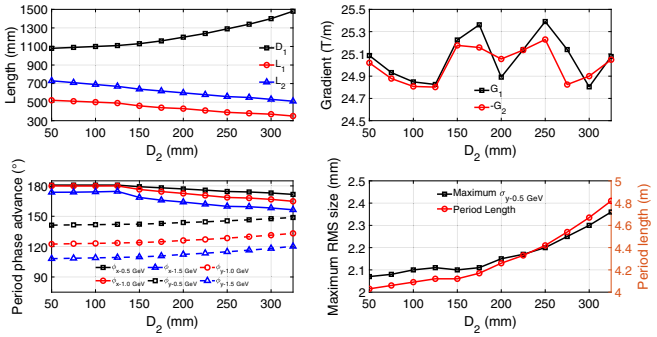

FIG. 6. Optimization on D_2 and D_1. (With D_2 increases, D_1 is increasing, while L_1 and L_2 are decreasing; the gradient is limited within 25 ± 0.5 T/m; periodic phase advance increases in Y plane and decreases from about 180° in X plane; beam maximum RMS size and period length are increasing roughly.)

and Q_2 almost the same. For a fixed drift length D_2 between the quadrupoles in the triplet, there is a minimum length for D_1 before the triplet in a period for keeping the stable periodic envelope. Considering backward

TABLE III. Parameters for different proton energies in VDS for $\begin{cases} D_1 = 1130 \text{ mm} \\ D_2 = 150 \text{ mm} \end{cases}$, $\begin{cases} L_1 = 460 \text{ mm} \\ L_2 = 640 \text{ mm} \end{cases}$, $\begin{cases} G_1 = 25.2248 \text{ T/m} \\ G_2 = -25.1764 \text{ T/m} \end{cases}$.

Parameters	Unit	Values		
Energy	MeV	500	1000	1500
Magnetic rigidity	T · m	3.636	5.657	7.507
$\beta\gamma$	…	1.162	1.808	2.399
Beam RMS size at the waist	mm	0.35	0.35	0.35
β function at the waist	mm/(π·mrad)	0.569	0.886	1.175
X periodic phase advance	°	179.2	176.5	168.6
Y periodic phase advance	°	142.2	124.0	109.8
Highest polar field strength	Gs	3927	5995	7567
Maximum RMS envelope	mm	2.10	1.44	1.15

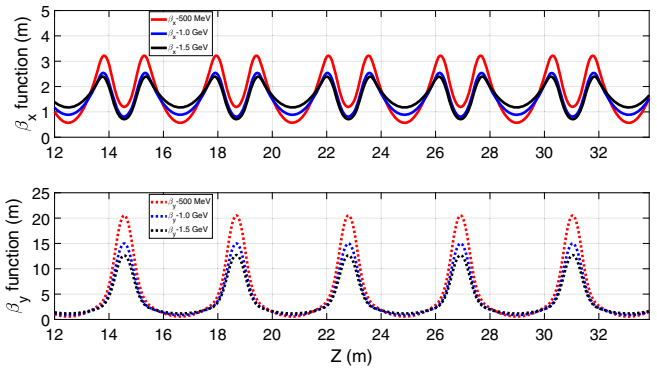

FIG. 7. β function in VDS. (Beam sizes are the same at vacuum holes for different energies. Since the geometric emittance for lower energy beam is larger, β function at the waist is smaller).

compatibility for energy, the ratio L_2/L_1 should be around 1.4 mainly based on 1.5 GeV beam, and it is also covered by lower energy cases, as shown in Fig. 5.

To optimize D_2 and D_1, the gradient of quadrupoles is limited within 25 ± 0.5 T/m with the radius of 30 mm, and the comparison results are shown in Fig. 6. Normally, thinner quadrupoles, smaller maximum RMS size, and shorter period length are preferred, so $D_2 = 150$ mm is chosen as the optimized value where there is a local minimum for beam maximum RMS size, and related parameters are listed in Table III. In that case, the polar field is within 8000 Gs for the highest energy, and the diameter of the VDS holes is chosen as 10 mm. Beam envelope and power density level are shown in Figs. 7 and 8 with different energies.

D. Collimation

Since the VDS holes are small, beam halo or off-center beam will lead to a large amount of power loss. To control beam losses at certain key locations, the separated function

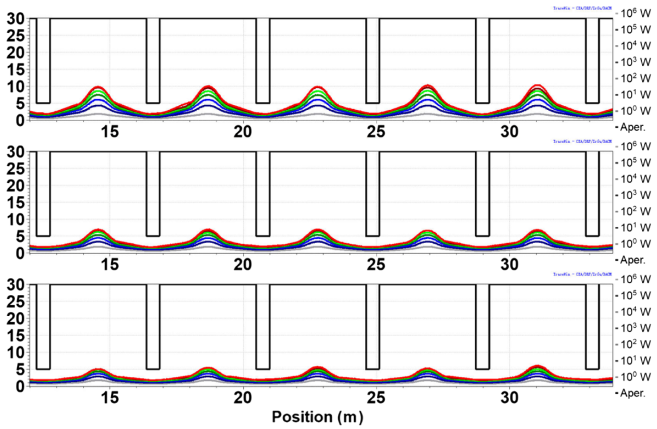

FIG. 8. Power density level in VDS. (Y-axis indicates radius in mm, from top to bottom: beam energy $E = 500$, 1000, 1500 MeV).

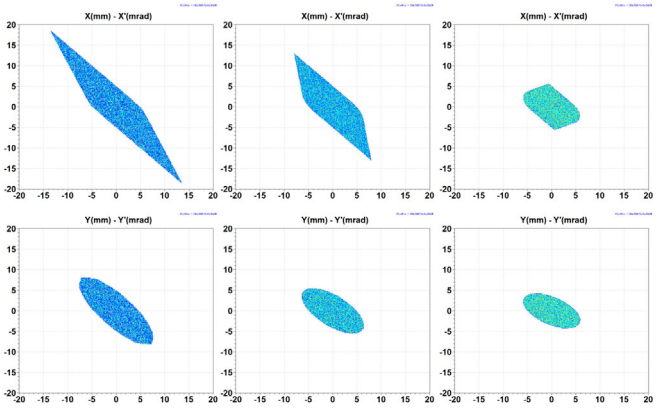

FIG. 9. Acceptance of VDS for different energies. To avoid too large position or angle in phase space, the acceptance calculation includes part of the matching section between the collimation and the VDS, i.e., from the end of the last quadrupole Q_5 of the matching section until the end of VDS. (From left to right: beam energy $E = 500$, 1000, 1500 MeV; the top is for X-X' and the bottom is for Y-Y')

of collimation and VDS are considered. Thus, no water cooling is considered in VDS holes, and the beam is collimated upstream of the VDS section.

The main function of the collimation section is to collimate the outer particles in the phase space to avoid them losing at the VDS holes, which means that the emittance of the beam at the exit of the collimation section should be well inside the acceptance of the VDS section. For full collimation, the total phase advance (or rotation in phase space) should be at least 180° in the collimation section. Figure 9 shows the acceptance of VDS for different energies. Since periodic phase advance in X plane for 500 MeV and 1 GeV are quite near to 180°, they look like deviated from the "elliptical" acceptance.

As shown in Fig. 9, the acceptance at 1.5 GeV is smaller than that at 500 MeV or 1 GeV, which is the object in the study below. For the same reason as mentioned in the VDS section, the triplet is chosen as the periodic structure in the collimation section. Different periodic phase advances are compared and optimized as shown in Table IV and 60° phase advance multiply 3 periods is adopted. The reason is as follows: 1. Comparing to 90° collimation, 60° collimation has much less particles outside of the desired emittance, as it has been discussed at CERN [22]; 2. With the increase of periodic phase advance, the number of periods and quadrupoles are decreasing. Thus, higher phase advance with shorter length and fewer quadrupoles is preferred from the cost view, as long as it meets the collimation requirements; 3. Larger radius of collimators is preferred based on the consideration of beam center offset, errors and the heat distribution on collimators; 4. The maximum beam size is acceptable both in the periodic section and matching section, while the polar field strength increases sharply with the increase of periodic

TABLE IV. Comparison of different periodic phase advance in the collimation section for 1.5 GeV beam.

Periodic phase advance	30°	36°	45°	60°	90°
Number of periods	6	5	4	3	2
Total length [m]	15	12.5	10	7.5	5
Number of quadrupoles	18	15	12	9	6
Collimators radius in X/Y planes [mm]	3.73/3.37	3.40/3.01	3.08/2.64	2.73/2.20	2.33/1.63
σ_{max} in periodic/matching section [mm]	0.82/1.07	0.77/1.00	0.72/0.99	0.69/1.01	0.70/1.11
$G_{max} \cdot R$ in periodic/matching section [Gs]	3701/5783	4417/5917	5464/6167	7126/6598	10041/7191
5σ envelope	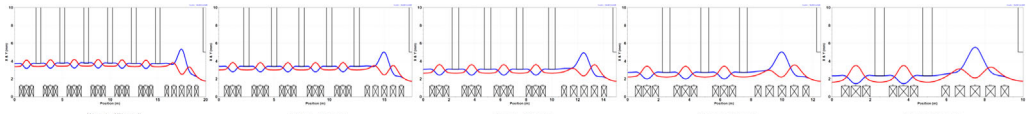				
Emittance edge X-X′	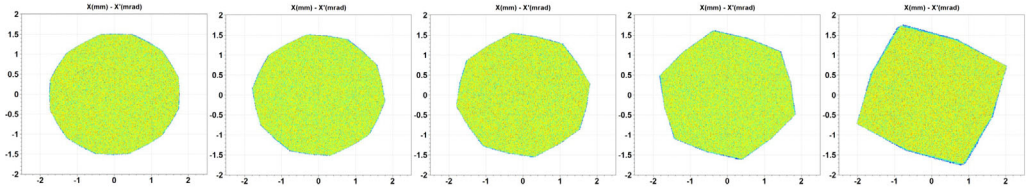				
Emittance edge Y-Y′	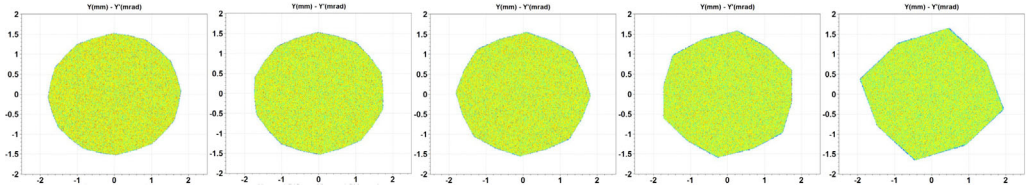				

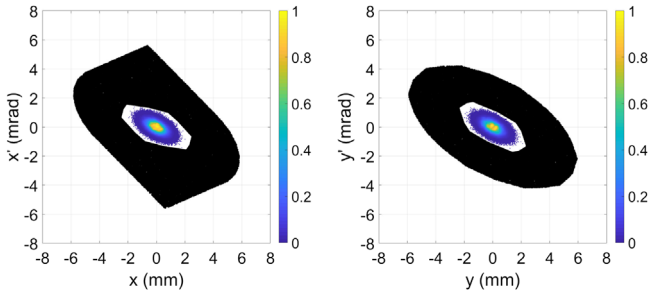

FIG. 10. Emittance of the collimation section and acceptance of the VDS section for 1.5 GeV beam. The dark area is the acceptance of VDS section. The white hexagonal area is the maximum beam emittance after collimation. Particles in blue and yellow colors are collimated beam emittance.

phase advance, and it is within 8000 Gs for the case of 60° phase advance.

From the view of emittance after the collimation section, $x_{\max}$ and $x'_{\max}$ are within 1.8 mm and 1.6 mrad for the cases with periodic phase advance of 60°. Balancing all the considerations mentioned above, $60° \times 3$ periods is adopted as the optimum choice in the collimation section.

To check the effectiveness of the collimation section, the emittance after the collimation section and the acceptance of the VDS section are put together, as shown in Fig. 10 for 1.5 GeV beam. The acceptance of VDS is about 7 times of the emittance edge of the collimation section.

E. Multiparticle tracking

The input distribution of the collimation section is chosen as 2D Gaussian distribution cutting at 6 standard deviations as shown in Fig. 11. The input normalized RMS emittance is $\varepsilon_{x/y/z} = 0.25/0.25/0.35\ \pi \cdot \text{mm} \cdot \text{mrad}$. To check the case with beam halo, 0.1% halo is added in the input distribution. The diameter of the 3 collimators is adjusted to $5.6\sigma/5.0\sigma/4.4\sigma$ to guarantee that the power loss on the collimators is evenly distributed.

Based on the optimized VDS and collimation section at 1.5 GeV energy, the 5σ envelope and power density

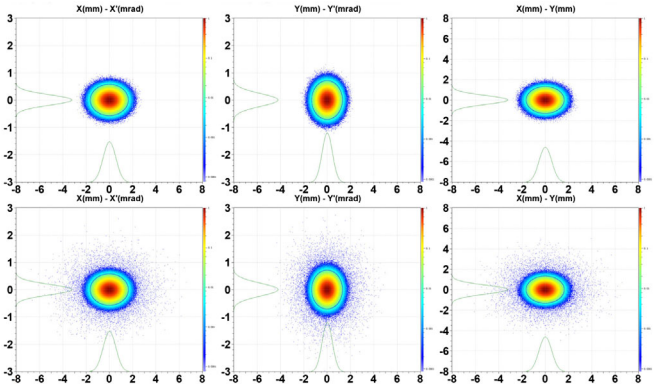

FIG. 11. Input distribution of collimation section. (Top for beam without halo, bottom for beam with 0.1% halo).

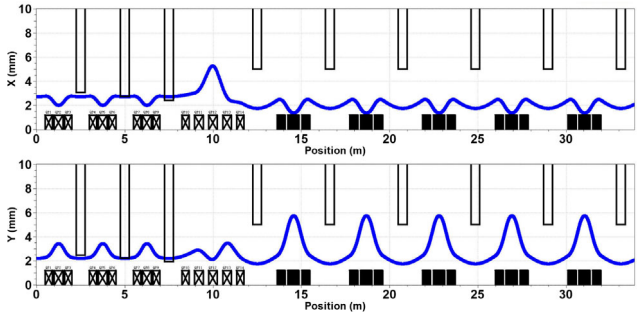

FIG. 12. 5σ envelope in optimized collimation and VDS section for 1.5 GeV beam.

distribution are shown in Fig. 12 and Fig. 13. Power losses on each collimator are about 10 W and 1.3 kW for the beam with and without the halo, and there is no power loss in the VDS section in all cases (Fig. 14).

Detailed sensitivity analysis on the input beam trajectories, manufacturing errors and alignment errors of collimators are studied. The criterion is based on the power loss on collimators. Since it is already at kW level, we assume that the power loss variation caused by errors should be within 10% of the designed maximum power loss on collimators. For trajectory errors, when the input beam center is shifted by 0.1 mm, or the input beam angle is shifted by 0.025 mrad, the power loss variation is about 2.5%. The same method is applied for the manufacturing errors and alignment errors of the collimators and the results are 0.05 mm and 0.2 mm respectively. When all the errors are applied in the lattice, the total power loss variation is within 10%, which is within the scope of demand. In general, the input beam trajectories should be within $dx/dy = \pm 0.1$ mm, $dx'/dy' = \pm 0.025$ mrad, and the manufacturing errors and alignment errors should be within ± 0.05 mm and ± 0.2 mm, respectively.

F. Feasibility

Beam dynamics are studied and optimized, including the hole aperture in the VDS section and periodic phase advance in the collimation section. Multiparticle tracking

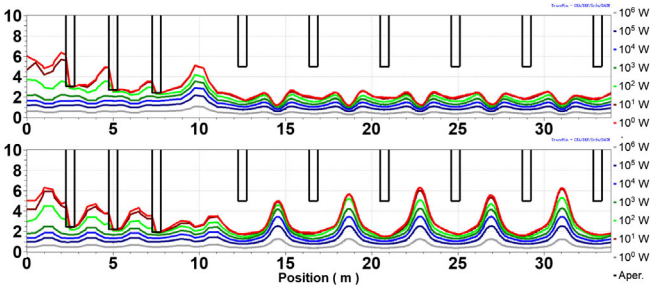

FIG. 13. Power density distribution in optimized collimation and VDS section for 1.5 GeV beam with 0.1% halo. (Top for X plane and bottom for Y plane).

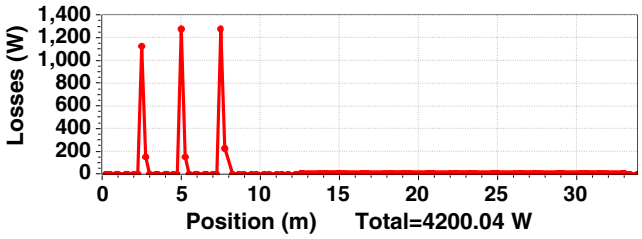

FIG. 14. Power loss distribution for the beam with 0.1% halo (about 1.3 kW for each collimator). No power loss in the VDS section.

with halo shows that no power lost in VDS holes, verifying the beam dynamics feasibility of vacuum differential system for the high-power windowless target of CiADS.

III. GAS SCATTER

A. Mechanism and method

As shown in Fig. 2, there is about 30 meters from the last vacuum hole to the target, which is filled with helium gas in 5×10^4 Pa (target zone), and another 30 meters with helium gas in about 100 Pa (transition zone). The proton helium scattering will lead to beam size increase and power loss on the beam tube.

As charged hadronic particle, proton will be scattered by helium nucleus due to Coulomb interactions and hadronic interactions when transporting in helium gas. Unlike hadronic elastic process, the Coulomb interaction between proton and helium usually leads to small-angle scattering. Because the beam tube is quite slender, single hadronic elastic scattering can easily lead to the loss of the particle, while the effect of Coulomb scattering will accumulate along the long tube, resulting in a considerable overall loss rate. The longer the beam tube is, the more significant the accumulated effect will be. Thus, both Coulomb scattering and hadronic process should be taken into consideration carefully.

The gas scattering effect is investigated base on the Monte Carlo simulation using GEANT4.10.6 [23] in this section. For Coulomb scattering process, the WVI-SS [24,25] model which naturally combines the Wentzel-VI multiple scattering model [23,24] and the single scattering model based on Wentzel scattering function [26] is used. The Wentzel-VI model is for precise simulation of muons and hadrons. The combination of single and multiple scattering models presents precise description of Coulomb scattering effect even in low-density media.

As for hadronic elastic process, the G4ChipsElasticModel [23] based on CHIPS approach [27] is adopted. It was shown [23] that the CHIPS model is the most reliable one among all of the four options exist in GEANT4 for simulation of proton-nucleus elastic scattering at medium and high energy protons.

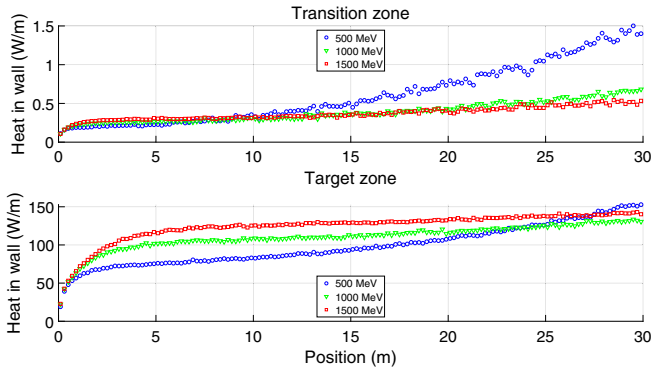

FIG. 15. Power loss on the beam tube for different energies in transition and target zone.

B. Simulation

The simulation is based on the beamline near the target, with helium vacuum pressure of 5×10^4 Pa and 100 Pa for 5 mA proton beam, as shown in Fig. 2. The beam tube is 316 stainless steel with 5 mm thick. Without scattering, beam RMS size is about 5.5 mm for transition zone and 19 mm on the target for Gaussian distribution.

In the transition zone where the vacuum is about 100 Pa, the maximum power loss on the tube is within 1.5 W/m (Fig. 15), and it is human maintainable in this zone.

As shown in Fig. 16, beam loss is mainly caused by Coulomb scattering in transition zone, but it still stays at several W/m level. In the target zone, beam power loss is dominated by Hadronic elastic process, up to several hundred W/m, which is far higher than 1 W/m hands-on maintenance level in the accelerator [28]. Thus, the remote control is required in this zone due to the high radiation dose rate.

The gas scattering will also lead to beam size increase. The effect of gas scattering on beam size increase in the transition zone is neglectable, and it increases 18% in the worst case for the 500 MeV beam in the target zone. For circular scan, extra power loss on the tube contributed by beam size increase is 47 W, 7.5 W, 6.8 W for the three different energies. Since there would be cooling on the tube before the target, dozens of watts loss would be acceptable. To decrease the effect, smaller beam size on the target or larger beam tube near the target are considered. If the designed beam RMS size on the target decreases by 1 mm,

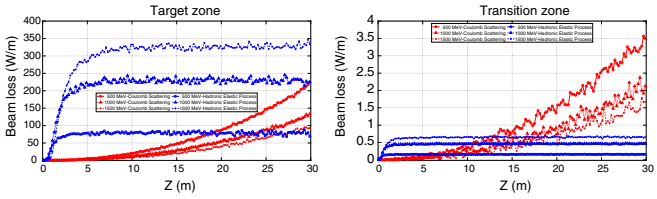

FIG. 16. Beam loss caused by gas scattering in transition and target zone.

or the radius of beam tube increases by 5 mm, the power loss will decrease sharply from 47 W to 17 W for the 500 MeV beam.

C. Feasibility

In the transition zone with the vacuum level of about 100 Pa, beam loss and beam size increase are acceptable. In the target zone, the gas scattering effect is serious, and a dedicated radiation-hard design and remote control need to be considered in that region, and beam size should be controlled smaller or beam tube larger to balance the beam size increase caused by gas scattering for low energy beam.

IV. VACUUM DIFFERENTIAL TEST

A. System setup

A prototype for the vacuum differential system with 6 stages is designed and tested at the Institute of Modern Physics, Chinese Academy of Sciences, as shown in Fig. 17. Taking the above simulation results, long thin tubes with a diameter of 10 mm is chosen at the 1st, 2nd, and 3rd stages, and small holes with the same diameter is chosen at the rest stages of VDS, as shown in Fig. 18. AISI304 stainless steel is chosen as the material of vacuum chambers and the leakage rate is within 1×10^{-10} mbar $\cdot$ L/s. All the chambers and tubes are mirror polished, pickled, ultrasonic cleaned and high temperature degassed before the test.

Considering the ratio of the diameter of the tube and the mean free path (MFP) of the molecules of hydrogen or helium, it is viscous flow in the 1st and 2nd VDS stages, Knudsen flow in the 3rd stage, and molecular flow in the 4th, 5th, and 6th stages. Different pumps and gauges are chosen based on the flow type in different stages, as shown in Table V.

B. Test result

In the test, the vacuum transition from 5×10^4 Pa to 7.8×10^{-5} Pa was achieved in the multistage VDS for Helium gas for the long-term test, as shown in Fig. 19 (Left). When considering vacuum variation in the plenum chamber for the limit test, the vacuum at the 6th stage will become much worse when the vacuum pressure in the plenum chamber is beyond 8×10^4 Pa. The same test for Nitrogen gas was also conducted and the best vacuum at the

FIG. 17. The layout of the VDS prototype.

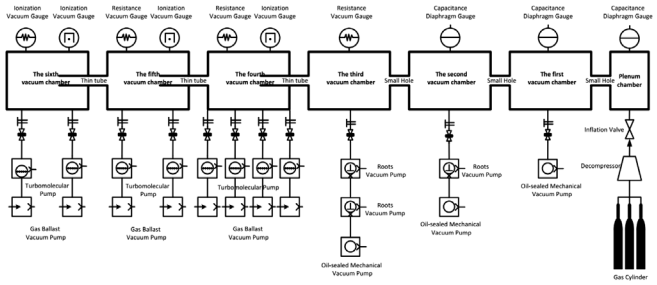

FIG. 18. The sketch of the VDS prototype.

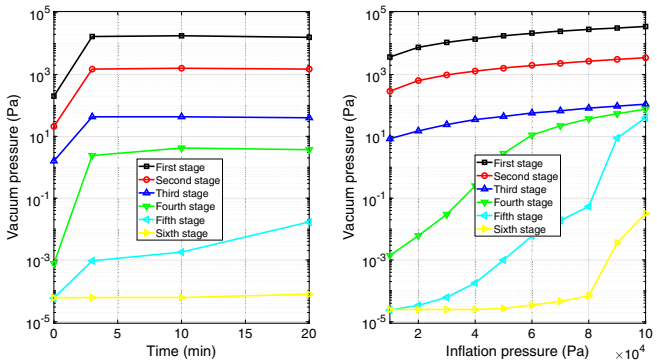

FIG. 19. Vacuum test results for Helium gas in VDS. (Left is for a long-term test: vacuum pressure in the plenum chamber stays at 5×10^4 Pa; Right is for the limit test: vacuum pressure in the plenum chamber varies from 1×10^4 Pa to 1×10^5 Pa gradually; the six lines from top to bottom: the first to the sixth stage of VDS).

6th stage VDS reached 2.5×10^{-5} Pa, and it is about half order lower than the case with Helium gas, which agrees with the fact that the Nitrogen molecule size is larger than Helium and it is easier to be pumped out. Figure 20 shows the comparison results with the different types of gas and initial pressure in the plenum chamber.

For nitrogen, it is easy to realize about 10 orders of magnitude vacuum transition from 1×10^5 Pa to 2.5×10^{-5} Pa

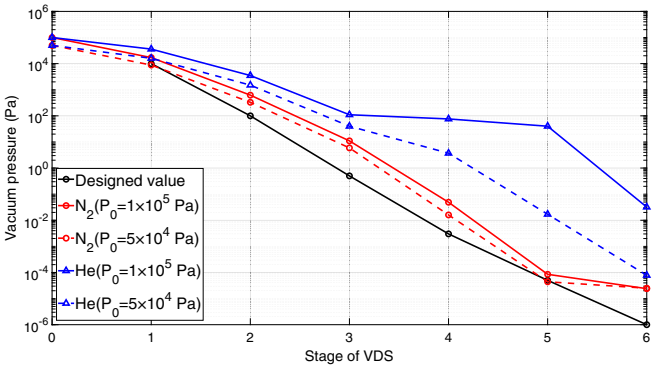

FIG. 20. Vacuum comparison with different initial pressure and gas in VDS. (Nitrogen gas: from 1×10^5 Pa to 2.4×10^{-5} Pa, Helium gas: from 8×10^4 Pa to 7.8×10^{-5} Pa)

TABLE V. Flow type, gauges and pumps in the test of VDS.

Stage	Flow type	Vacuum gauge	Pump type
0[a]	Viscous flow	Diaphragm gauge	…
1	Viscous flow	Diaphragm gauge	Oil pump
2	Viscous flow	Diaphragm gauge	Roots pump
3	Knudsen flow	Pirani gauge	Roots pump
4–6	Molecular flow	Cold cathode gauge	Molecular pump

[a]Stage 0 means the plenum chamber (as shown in Fig. 18).

in both long-term test and limit test. For helium, it would be 3.2×10^{-2} Pa at the 6th stage if it is 1×10^{5} Pa in the plenum chamber, however, as long as it keeps lower than 8×10^{4} Pa in the plenum chamber, the vacuum in the 6th stage of VDS could reach 7.8×10^{-5} Pa.

C. Feasibility

The result of the vacuum differential test indicates that about 10 orders of vacuum transition is achieved from 1×10^{5} Pa to 2.5×10^{-5} Pa for nitrogen gas, and 9 orders from 8×10^{4} Pa to 7.8×10^{-5} Pa for helium gas.

In the test, the tube length is 120 mm and the periodic length is about 0.75 m. For further study, the tube length could be extended to 500 mm and the periodic length to 4.12 m, providing longer space for placing more pumps. The vacuum achieved at the 6th stage will also be better. If 4 K cold trap is added at the zero stage for absorbing the radioactive gases from the target and residual impurity gases in the transfer line, and liquid-nitrogen cold traps are added at the entrance of oil pumps in the 1st, 2nd, and 3rd stages to avoid oil pollution from pumps, it is also beneficial for the improvement of the vacuum differential system.

V. CONCLUSIONS

With the detailed simulation and optimization of the physical design for the vacuum transition at the HEBT of CiADS, a vacuum differential system is proposed with upstream collimators for the high-power windowless target. Based on the 2D Gaussian distribution, particles outside of 5σ are collimated to guarantee the emittance edge of the collimation section is well inside the acceptance of the VDS section, with acceptable power loss on collimators. The simulation shows that power loss from gas scattering is acceptable in the VDS system. The VDS test is conducted without beam and vacuum transition is achieved at the magnitude of 10^{-5} Pa, with possible improvement in the future. Based on the simulation and test results, a feasible solution for the HEBT to meet the vacuum requirement of the high-power windowless target is proposed. Some engineering problems are still to be studied for the high duty factor machine, including the reliability study related with vacuum, power loss, radioactive contamination boundaries, etc.

ACKNOWLEDGMENTS

This work is supported by CAS Strategic Priority Research Program-Future Advanced Nuclear Fission Energy (Accelerator-Driven Sub-critical System) [XDA03000000], the Large Research Infrastructures of 12th Five-Year Plan: China initiative Accelerator Driven System, and the National Natural Science Foundation of China (Grant No. 11805253).

[1] W. L. Zhan, Accelerator driven sustainable fission energy, in *Proceedings of the 7th International Particle Accelerator Conference, Busan, Korea, 2016* (JACoW, Geneva, 2016), pp. 4271–4275, https://doi.org/10.18429/JACoW-IPAC2016-FRYAA03.

[2] Z. J. Wang *et al.*, The status of CiADS superconducting LINAC, in *Proceedings of the 10th International Particle Accelerator Conference, Melbourne, Australia, 2019* (JACoW, Geneva, 2019), pp. 994–997, https://doi.org/10.18429/JACoW-IPAC2019-MOPTS059.

[3] Y. Lei and Z. Wenlong, New concept for ADS spallation target: Gravity-driven dense granular flow target, Sci. China Technol. Sci. **58**, 1705 (2015).

[4] F. C. Difilippo, Design and effects of the proton window of the Spallation Neutron Source, in *Advanced Monte Carlo for Radiation Physics, Particle Transport Simulation and Applications* (Springer, Berlin, Heidelberg, 2001), pp. 1009–1014, https://doi.org/10.1007/978-3-642-18211-2_162.

[5] J. R. Haines, T. J. McManamy, T. A. Gabriel, R. E. Battle, K. K. Chipley, J. A. Crabtree, L. L. Jacobs, D. C. Lousteau, M. J. Rennich, and B. W. Riemer, Spallation neutron source target station design, development, and commissioning, Nucl. Instrum. Methods Phys. Res., Sect. A **764**, 94 (2014).

[6] S.-i. Meigo, M. Ooi, M. Harada, H. Kinoshita, and A. Akutsu, Radiation damage and lifetime estimation of the proton beam window at the Japan Spallation Neutron Source, J. Nucl. Mater. **450**, 141 (2014).

[7] S. I. Meigo *et al.*, High Power Target Instrumentation at J-PARC for Neutron and Muon Sources, in *Proc. 57th ICFA Advanced Beam Dynamics Workshop on High-Intensity and High-Brightness Hadron Beams (HB16), Malm, Sweden, Jul. 2016* (JACoW, Geneva, 2016), pp. 391–396, https://doi.org/10.18429/JACoW-HB2016-WEPM2X01.

[8] H.-J. Wang, W.-B. Liu, H.-M. Qu, D.-H. Zhu, N. Huang, L. Kang, and R.-H. Liu, Thermal analysis and optimization of proton beam window for the CSNS, Chin. Phys. C **37**, 077001 (2013), https://doi.org/10.1088/1674-1137/37/7/077001.

[9] H. J. Wang, L. Kang, R. H. Liu, H. Qu, and D. H. Zhu, The design and analysis of proton beam window for CSNSIII, in *Proc. 4th Int. Particle Accelerator Conf. (IPAC13), Shanghai, China, May 2013* (JACoW, Geneva, 2013), paper THPFI032, pp. 3367–3369, https://accelconf.web.cern.ch/IPAC2013/papers/thpfi032.pdf.

[10] F. W. Wang, T. J. Liang, W. Yin, Q. Z. Yu, L. H. He, J. Z. Tao, T. Zhu, X. J. Jia, and S. Y. Zhang, Physical design of target station and neutron instruments for China Spallation Neutron Source, Sci. China Phys. Mech. Astron. **56**, 2410 (2013).

[11] Y. Dai, J. Henry, T. Auger, J.-B. Vogt, A. Almazouzi, H. Glasbrenner, and F. Groeschel, Assessment of the lifetime of the beam window of MEGAPIE target liquid metal container, J. Nucl. Mater. **356**, 308 (2006).

[12] F. Groeschel, C. Fazio, J. Knebel, Ch. Perret, A. Janett, G. Laffont, L. Cachon, T. Kirchner, A. Cadiou, A. Guertin, and P. Agostini, The MEGAPIE 1 MW target in support to ADS development: Status of R&D and design, J. Nucl. Mater. **335**, 156 (2004).

[13] Bubelis, Evaldas and Coddington, Paul and Leung, Waihung, Pre-Test Analysis of the MEGAPIE Spallation Source Target Cooling Loop Using the TRAC/AAA Code, in *Proceedings of the 2006 International Congress on Advances in Nuclear Power Plants (ICAPP '06)*, 2006, https://www.psi.ch/sites/default/files/import/fast/PublicationsEN/FB-DOC-06-004.pdf.

[14] C. Fazio, R. Stieglitz, J. U. Knebel, F. Groeschel, W. Wagner, A. Strinning, H. Heyck, Y. Dai, B. B. N. Smith, W. Leung, G. Laffont, T. Kirchner, A. Guertin, P. Agostini, D. Gorse, T. Auger, and J. B. Vogt, The MEGAPIE-TEST Project, in *International Workshop on P&T and ADS Development, Mol, Belgium, August 2003*, http://hal.in2p3.fr/file/index/docid/52528/filename/MEGAPIE-TEST_Project_2003_GA.pdf.

[15] Y. Dai and P. Marmy, Charpy impact tests on martensitic/ferritic steels after irradiation in SINQ target-3, J. Nucl. Mater. **343**, 247 (2005).

[16] Y. Dai, C. Fazio, D. Gorse, F. Gröschel, J. Henry, A. Terlain, J.-B. Vogt, T. Auger, and A. Gessi, Summary on the preliminary assessment of the T91 window performance in the MEGAPIE conditions, Nucl. Instrum. Methods Phys. Res., Sect. A **562**, 698 (2006).

[17] D. Uriot and N. Pichoff, Status of TraceWin code, in *Proc. 6th Int. Particle Accelerator Conf. (IPAC15), Richmond, VA, USA, May 2015* (JACoW, Geneva, 2015), pp. 92–94, https://doi.org/10.18429/JACoW-IPAC2015-MOPWA008.

[18] D. J. Hucknall, Introduction, in *Vacuum Technology and Applications* (Butterworth-Heinemann, Washington, DC, 1991), Chap. 1, p. 10.

[19] D. Daoan, Pipeline conductivity calculation, in *Vacuum Design Handbook* (National Defence Industry Press, Beijing, 2004), Chap. 2, pp. 101–124 (In Chinese).

[20] N. Catalan-Lasheras, Y. Y. Lee, H. Ludewig, N. Simos, and J. Wei, Optimization of the collimation system for the Spallation Neutron Source accumulator ring, Phys. Rev. Accel. Beams **4**, 010101 (2001).

[21] T. P. Wangler, Transverse particle dynamics, in *RF Linear Accelerators* (John Wiley & Sons, New York, 2010), Chap. 7, p. 222.

[22] J. B. Jeanneret, Optics of a two-stage collimation system, Phys. Rev. Accel. Beams **1**, 081001 (1998).

[23] J. Allison, K. Amako, J. Apostolakis, P. Arce, M. Asai, T. Aso, E. Bagli, A. Bagulya, S. Banerjee *et al.*, Recent developments in GEANT4, Nucl. Instrum. Methods Phys. Res., Sect. A **835**, 186 (2016).

[24] V. N. Ivanchenko, O. Kadri, M. Maire, and L. Urban, GEANT4 models for simulation of multiple scattering, J. Phys. Conf Ser. **219**, 032045 (2010).

[25] A. Bagulya, J. M. C. Brown, H. Burkhardt, V. Grichine, S. Guatelli, S. Incerti, V. N. Ivanchenko, O. Kadri, M. Karamitros, M. Maire, K. Mashtakov, M. Novak, L. Pandola, P. G. Rancoita, D. Sawkey, M. Tacconi, and L. Urban, Recent progress of GEANT4 electromagnetic physics for LHC and other applications, J. Phys. Conf. Ser. **898**, 042032 (2017).

[26] Gr Wentzel, Zwei Bemerkungen über die Zerstreuung korpuskularer Strahlen als Beugungserscheinung, Z. Phys. **40**, 590 (1926).

[27] M. V. Kossov, Chiral-invariant phase space model, Eur. Phys. J. A **14**, 265 (2002).

[28] R. A. Hardekopf, Beam loss and activation at LANSCE and SNS, in *7th ICFA Miniworkshop on High Intensity High Brightness Hadron Beams: Beam Halo and Scraping*, pages 62–69, 8 2000, https://lss.fnal.gov/archive/2000/conf/Conf-00-185.pdf#page=64.